Observations of Coherent Transverse Wakes in Shoaling Nonlinear Internal Waves

Andrew J. Lucas^{a,b} and Robert Pinkel^a

^a Scripps Institution of Oceanography, University of California, San Diego, La Jolla, California ^b Department of Mechanical and Aerospace Engineering, University of California, San Diego, La Jolla, California

(Manuscript received 17 March 2021, in final form 18 February 2022)

ABSTRACT: Space- and time-continuous seafloor temperature observations captured the three-dimensional structure of shoaling nonlinear internal waves (NLIWs) off of La Jolla, California. NLIWs were tracked for hundreds of meters in the cross- and along-shelf directions using a fiber optic distributed temperature sensing (DTS) seafloor array, complemented by an ocean-wave-powered vertical profiling mooring. Trains of propagating cold-water pulses were observed on the DTS array inshore of the location of polarity transition predicted by weakly nonlinear internal wave theory. The subsequent evolution of the temperature signatures during shoaling was consistent with that of strongly nonlinear internal waves with a large Froude number, highlighting their potential to impact property exchange. Unexpectedly, individual NLIWs were trailed by a coherent, small-scale pattern of seabed temperature variability as they moved across the mid- and inner shelf. A kinematic model was used to demonstrate that the observed patterns were consistent with a transverse instability with an along-crest wavelength of ~10 m—a distance comparable to the cross-crest width of the wave core—and with an inferred amplitude of several meters. The signature of this instability is consistent with the span-wise vortical circulations generated in three-dimensional direct numerical simulations of shoaling and breaking nonlinear internal waves. The coupling between the small-scale transverse wave wake and turbulent wave core may have an important impact on mass, momentum, and tracer redistribution in the coastal ocean.

SIGNIFICANCE STATEMENT: Internal waves permeate the ocean and atmosphere. Their transport of energy and momentum plays a central role in the ocean as a physical system and mediates critical biogeochemical property exchange. In the coastal ocean, internal waves fuel the local ecosystem by redistributing nutrients and shape the local geomorphology by resuspending and transporting sediment. Despite these important impacts, a detailed understanding of nonlinear internal wave evolution in shallow water remains an elusive goal, limited by the difficulty of observing the process in action. Here we describe a transformative observational approach to track internal waves through shoaling to dissipation, combining fiber optic distributed temperature sensing and ocean-wave-powered vertical profiling to track individual waves continuously in the cross- and along-shelf direction. The waves arise from the locally energetic internal tide and undergo rapid nonlinear transformation in the shallow waters of the inner shelf. Our measurements provide the first observational evidence that after evolving into highly nonlinear waves of elevation, the waves develop a trailing, wake-like, three-dimensional instability. This instability resembles the vortical coherent structures generated in high resolution numerical simulations of internal wave shoaling, previous observations of related phenomena in the atmosphere, and in breaking surface gravity waves. The observed transverse structure has an along-crest wavelength of only ~10 m, making it nearly invisible to traditional ocean sampling techniques. The generation of coherent vortical structures during internal wave shoaling may have a profound influence on the exchange of energy, nutrients, and sediments in coastal oceans and lakes globally.

KEYWORDS: Coastal flows; Internal waves; In situ oceanic observations; Profilers, oceanic; Nonlinear dynamics; Solitary waves

1. Introduction

On a calm day offshore of Southern California, shore-parallel bands of alternating sea surface roughness can stretch for kilometers along the coast (e.g., Ewing 1950). These signatures are the ocean surface expression of nonlinear internal waves (NLIWs), a common phenomenon in open oceans, marginal seas, and lakes around the world (Liu et al. 1998; Jackson and Apel 2004; Helfrich and Melville 2006; Lamb 2014; Boegman and Stastna 2019). Offshore of the Scripps Institution

Openotes content that is immediately available upon publication as open access.

Corresponding author: A.J. Lucas, ajlucas@ucsd.edu

of Oceanography (SIO) Pier, in La Jolla, California, the sea surface bands march slowly onshore and disappear as the underlying internal wave train shoals into shallow water (Winant 1974).

Just as surface waves deposit energy and momentum into the surfzone, shoaling nonlinear internal waves drive mixing, property exchange, and residual currents as they shoal and dissipate near the coast (e.g., Klymak and Moum 2003; Bourgault et al. 2008; Shroyer et al. 2010; Hamann et al. 2018; Colosi et al. 2018; McSweeney et al. 2020; Jones et al. 2020). Correspondingly, internal wave-mediated turbulence and mixing are of first-order importance to a number of coastal ocean processes, including ecosystem structure and function (e.g., Pineda 1999; Sharples et al. 2007; Lucas et al. 2011), coastal geomorphology, and sediment dynamics (e.g., McPhee-Shaw and Kunze 2002; Bourgault et al. 2014; Boegman and Stastna 2019). Despite the importance of internal wave transformation in shallow water,

DOI: 10.1175/JPO-D-21-0059.1

questions remain about the details: how do the dynamics that lead to the turbulent dissipation of shoaling internal wave energy play out over the inner shelf?

NLIW evolution in shallow water has been evaluated from moorings that provide the time evolution of the water column's vertical structure (e.g., density as a function of depth and time), but such information can only be gathered a few discrete horizontal locations simultaneously. Shipboard surveys can capture snapshots of shoaling waves (e.g., density as a function of depth and distance), but there are practical limits on the number of such snapshots that can be acquired over the relatively short period of shoaling. Because of this fundamental trade-off, the observational study of shoaling NLIWs in the field has suffered from the difficultly in documenting the time-evolving horizontal structure of the process.

There are reasons to expect that NLIW shoaling in the coastal ocean is three-dimensional and small scale. Direct and large-eddy numerical simulations of internal wave shoaling and breaking includes the emergence of coherent vortical structures when the simulations are run in three dimensions rather than two (Stastna and Lamb 2002; Venayagamoorthy and Fringer 2005; Diamessis and Redekopp 2006; Gayen and Sarkar 2011; Arthur and Fringer 2014; Xu et al. 2016). These simulations suggest that during the wave steepening process, nonlinear instabilities occur involving either the leading or trailing wave face. As the instabilities evolve, a transverse "wake" can appear, often taking the form of a train of vortices of alternating sign with axes parallel to the direction of wave propagation (Gayen and Sarkar 2011; Arthur and Fringer 2014; Xu et al. 2016). Qualitatively similar coherent vortical structures are also found in breaking surface waves (Watanabe et al. 2005), free shear layers (Bernal and Roshko 1986; Lasheras and Choi 1988), and the atmosphere (Fritts et al. 1994). In those contexts, the coherent structures influence the energetics, mixing, and property exchange in the fluid. While the development of three-dimensional coherent instabilities during NLIW shoaling is suggested by numerical simulations, these dynamics have not yet been documented below the ocean's surface.

In what follows, we present a dense set of observations gathered offshore of La Jolla, California, that document the NLIW shoaling process continuously in time and space. The measurements were gathered by a combination of approaches: a fiber optic distributed temperature sensing (DTS) array that measured the sea-bottom temperature structures generated by shoaling internal waves, and an ocean-wave-powered Wirewalker autonomous profiling mooring that mapped the complex vertical and temporal variability of the stratified waters through which these internal waves moved. These observations elucidated the multiscale process that connected the energetic internal tide to the three-dimensional shoaling and dissipation of trains of highly nonlinear internal waves across the inner shelf.

2. Physical setting and observations

a. Setting

The semidiurnal internal tide is a dominant component of the physical ocean variability in the stratified waters over the California inner shelf (Lerczak et al. 2003; Nam and Send 2011; Buijsman et al. 2012; Johnston and Rudnick 2015). Offshore, baroclinic tides are generated by interaction of the barotropic tides and steep bathymetry (Ponte and Cornuelle 2013), and subsequently propagate to the continental slope and shelf. As the internal tide impinges on the coastal bathymetry, reflection (Lerczak et al. 2003; Alberty et al. 2017) and nonlinear processes (Walter et al. 2012; McSweeney et al. 2020) transform the linear internal tide into a complex superposition of vertical modes, scatter energy to different frequencies and wavelengths, and drive turbulence, mixing, and property exchange (Becherer et al. 2020; Hamann et al. 2021).

At the study site in La Jolla, California, nonlinear internal waves of tidal frequency were documented by Winant (1974) from measurements at the end of Scripps Pier. Subsequently, Sinnett et al. (2018) showed that NLIWs of tidal and tidal-harmonic frequencies could be tracked across the mid and inner shelf, occasionally reaching past the pier end into the surf zone. These waves were described as "bore-like," in analogy to similar wave forms observed in central California (Walter et al. 2014; Spydell et al. 2021), the Oregon continental shelf (D'Asaro et al. 2007), and elsewhere (Alford et al. 2015; Hamann et al. 2018). At times, trains of high-frequency (6–10 cph) NLIWs were found to be superimposed over the lower-frequency internal tide (e.g., Fig. 5e in Sinnett et al. 2018). In waters shallower than 10-m depth, however, those high-frequency NLIWs were largely absent.

While Sinnett et al. (2018) inferred that dissipation over the inner shelf was important to the dynamics of the NLIWs at tidal and higher frequencies, the pathway of energy from NLIWs to mixing was not captured. Just 5 km offshore, within the La Jolla submarine canyon, Alberty et al. (2017) and Hamann et al. (2021) showed that upward of 90% of the incident internal tide energy was reflected, with the remaining energy largely dissipated within the canyon itself. Similarly, a comprehensive study ~30 km to the south, away from the influence of the La Jolla submarine canyon, showed that the coastal semidiurnal internal tide was also predominately reflected, but that NLIWs at frequencies higher than several cycles per hour moved across the shelf and appeared to dissipate over the inner shelf (Lerczak 2000; Lerczak et al. 2003). The fate of these energetic, high frequency NLIWs over the inner shelf-including their relationship to the local internal tide, and the phenomenology of their dissipation—are the primary concerns of this manuscript.

b. Observations

To document NLIW shoaling in shallow water, we deployed a Silixa ULTIMA-SE fiber optic DTS array off SIO Pier, provided by Oregon State University Center for Transformative Environmental Monitoring Programs (https://ctemps.org/). The DTS array was deployed from 25 June to 23 August 2013, spanning a depth range of 5–90 m (Fig. 1a). Distributed temperature sensing is a transformative tool for measuring nonlinear internal wave evolution, providing range- and time-continuous estimates of temperature over-fiber optic cables of up to 2-km length (Selker et al. 2006;

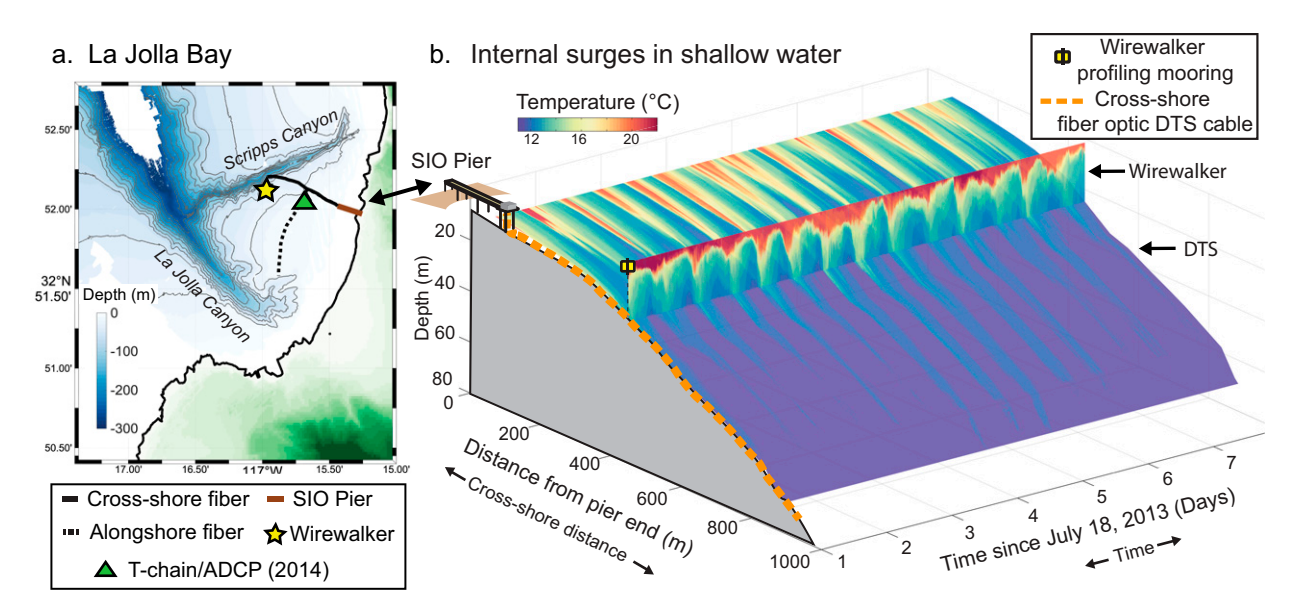


FIG. 1. (a) The fiber optic DTS array was deployed from Scripps Pier, with a cross-shore cable running offshore from the pier end for ~ 800 m (solid black line) and an L-shaped alongshore cable following the first until the 22-m isobath, where it was turned to the south and extended parallel to the shore for an additional ~ 1 km (dotted black line). The location of the Wirewalker (star) and T-chain/ADCP (triangle) are indicated. (b) Seven days of concurrent Wirewalker (vertical curtain) and DTS (seabed) temperature measurements from the cross-shore leg of the fiber optic array. The SIO Pier is shown to scale.

Tyler et al. 2009; Connolly and Kirincich 2019; Davis et al. 2020).

Two fibers were installed on the seafloor off of SIO Pier and sampled simultaneously. A "cross-shore" multimode fiber optic cable was extended ~900 m from the pier end directly offshore. A second, ~1800-m-long L-shaped "alongshore" cable extended first from the pier end to the 22-m isobath, and then followed the 22-m isobath toward the south, parallel to the coastline (Fig. 1a).

The DTS temperature observations were calibrated by the use of diver-deployed oceanographic-quality thermistors collocated with each fiber at various ranges (see also Sinnett et al. 2020). The corrected observations had approximately 0.1°C root-mean-square temperature (RMS) precision (appendix A; Fig. A1). The base 0.6 m by 20 s range-time resolution measurements were used to investigate individual shoaling waves. Further averaging in space and time to 2 m and 1 min generated temperature observations with an RMS temperature precision of 0.03°C. These were used in the statistical analyses. The performance of the DTS relative to calibrated oceanographic sensors is consistent with the findings of Sinnett et al. (2020), and showed the instrument is capable of measuring the temperature fluctuations of several degrees that are analyzed here (Fig. 1b).

To augment the DTS observations, a moored Wirewalker wave-powered vertical profiler (Rainville and Pinkel 2001; Pinkel et al. 2011; Lucas et al. 2017) was deployed on the 50-m isobath from 3 July to 5 August 2013 (Fig. 1a). The WW mooring collected more than 4000 full-depth profiles of temperature, salinity, chlorophyll a fluorescence, and currents at 4.5-min intervals over 31 days. Density was computed for each profile

over 0.5-m vertical spacing from 2 m above the seabed to 1 m below the sea surface. These high-resolution measurements of stratification were used to quantify the time variability of the inner shelf waveguide due to the internal tide, as described below

In 2014, the site was revisited. A simple mooring consisting of a 15-m thermistor chain (T-chain) and seafloor-mounted, upward-looking 1-MHz 5-beam ADCP (RD Instruments Sentinel V) was deployed on the 18-m isobath (Sinnett et al. 2018). The mooring was located \sim 50 m from the position of the turn in the alongshore fiber optic cable the year prior (Fig. 1a). The T-chain was instrumented with 15 SBE-56 thermistors sampling at a rate of 2 Hz and separated by 1 m vertically. These temperature observations in time were used to calculate the vertical position of isotherms with higher temporal resolution than the 2013 Wirewalker deployment afforded. The bottom-mounted ADCP was configured for 25-cm vertical bins and a 2-Hz ping rate. All pings were recorded in beam coordinates, and processed into an Earth-referenced coordinate system using the internal compass and pitch and roll sensors.

3. Results

a. Space-time scales of the observed internal wave field

Internal waves at tidal frequencies were the dominant signal in our summertime observations, driving vertical oscillations of the thermocline of \sim 50% of the water depth at midshelf over approximately 12 h (vertical curtain in Fig. 1b). This semidiurnal heaving of the thermocline corresponded to 300–400-m horizontal excursions of the thermocline across

the inner shelf seafloor (DTS seafloor measurements in Fig. 1b). Occasionally, the internal tide was observed to transport subthermocline water inshore of the pier end.

Spectral analysis of the seabed DTS temperature measurements documented that the tidal-band fluctuations were consistent with a partially reflected internal tide (Fig. 2). A wavenumber–frequency spectrum was calculated by forming 4 M2 (4 × 12.44 h) period overlapping segments in time (each treated with a Hamming window in time), and performing a two-dimensional FFT for each time segment across all ranges. After normalization, this yielded a wavenumber–frequency power spectral density estimate with one cycle per kilometer wavenumber resolution, estimated across the full internal-wave frequency bandwidth (i.e., ~1 cycle per day to 10 cycles per hour) at 58 degrees of freedom.

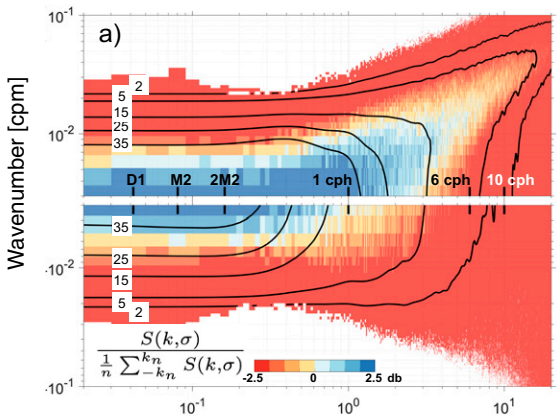
The onshore-offshore asymmetry of wave propagation was apparent in the difference in spectral levels between positive (onshore) and negative (offshore) wavenumbers at each frequency. This anisotropy is quantified in Fig. 2b, where the ratio of the onshore propagating to offshore propagating energy is shown. At tidal frequencies, the near-symmetry in the energy at onshore and offshore wavenumbers indicated that 80%–90% of the energy at tidal frequencies was reflected.

The reflecting internal tide led to a complex cycle of thermocline straining over the inner shelf, similar to that documented in the nearby La Jolla Canyon (Alberty et al. 2017; Hamann et al. 2021). On the seafloor, mode-1 vertical variability appeared as a cyclic onshore/offshore displacement of the thermal field (sloped arrows in Fig. 3a), while mode-2 vertical variability was seen as an alternating sharpening and broadening of the thermocline (vertical arrows in Fig. 3a). These modes were phase locked such that the thermocline sharpened as the baroclinic crest arrived.

When the thermocline became sufficiently sharp and steep, regular surges of cold water—occurring roughly every 10 min and separated in cross-shore dimension by approximately 100 m—could be tracked across the seafloor with the DTS fiber array (black star in Fig. 3a). Over a tidal cycle, a dozen or more regularly spaced and timed surges were often apparent (e.g., from 12 to 24 h in Fig. 3a). Unlike the tidal frequencies, the spectral analysis showed that variance at the periods and wavelengths corresponding to these surges was almost entirely onshore polarized (Fig. 2b).

The densely spaced fast-sampling thermistors and 5-beam ADCP deployed in 2014 resolved the vertical structure of high-frequency NLIW trains with similar characteristics to the seafloor surges measured on the DTS the previous year. For example, over a selected half tidal cycle, nearly two dozen individual oscillations passed the mooring over a three hour time period (Figs. 3b-d). The displacements associated with waves in the passing train were ~5 m (in 18-m depth), and the initial waves of the train coincided with the crest of the internal tide (Fig. 3b). As the thermocline descended with the ebbing internal tide, and the layer below the thermocline became thinner than the layer above, the high-frequency wave form measured at the mooring transitioned to that of a wave of elevation. The cold cores of individual NLIWs waves of elevation were associated with onshore-directed velocities

Normalized Power Spectral Density [db]



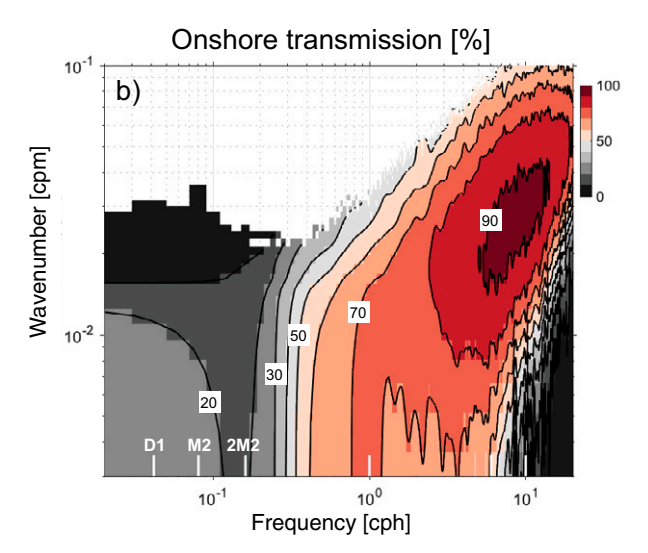


FIG. 2. (a) A normalized two-dimensional wavenumber-frequency spectrum indicates the increasing preference for shoreward propagation at frequencies above ~0.5 cph. The positive wavenumber direction is along the cable from the offshore end toward SIO pier. The spectra are normalized according to $S_{xx}(k,\sigma)/[(1/n)\sum_{k_0}^{k_n}S_{xx}(k,\sigma)]$, where S_{xx} is the wavenumber spectra at each frequency, k_n is wavenumber with a subscript n referring to resolved wavenumber bands. (b) The ratio of the onshore to offshore spectral density power is a measure of transmissivity of the inner shelf as a function of internal wave wavenumber and frequency, i.e., Transmission $\%(\sigma, ||k||) = \{1 - [S(\sigma, k -)/S(\sigma, k +)]\} \times 100$.

near the seabed, and strong (up to $10~{\rm cm~s}^{-1}$) vertical velocities preceding (upward) and following (downward) the wave crest (Figs. 3c,d).

b. The inner shelf waveguide

The appearance and form of the NLIW trains that occurred over the inner shelf can be compared to the expectations of weakly nonlinear theory (Shroyer et al. 2009). In our study area, the flat bottom assumption of the traditional

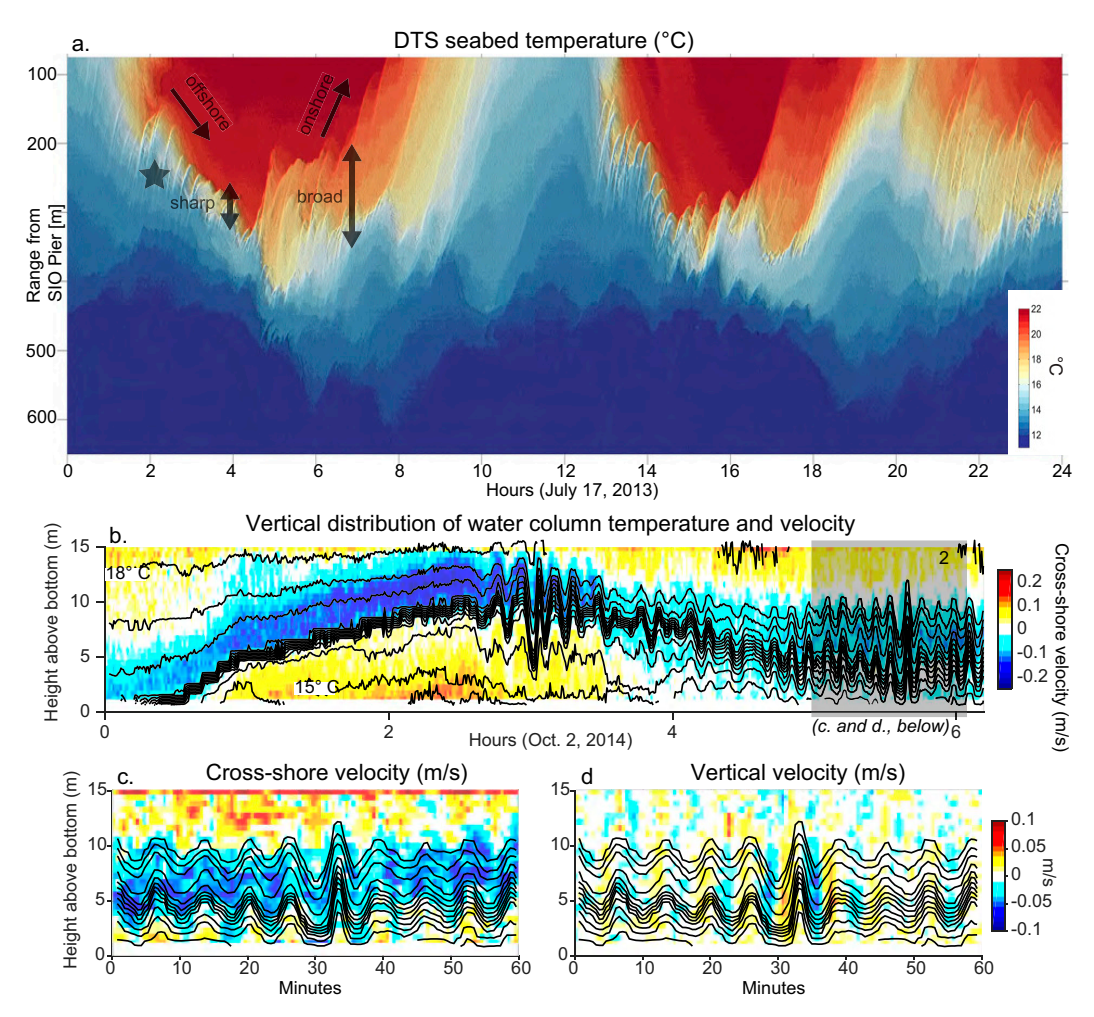


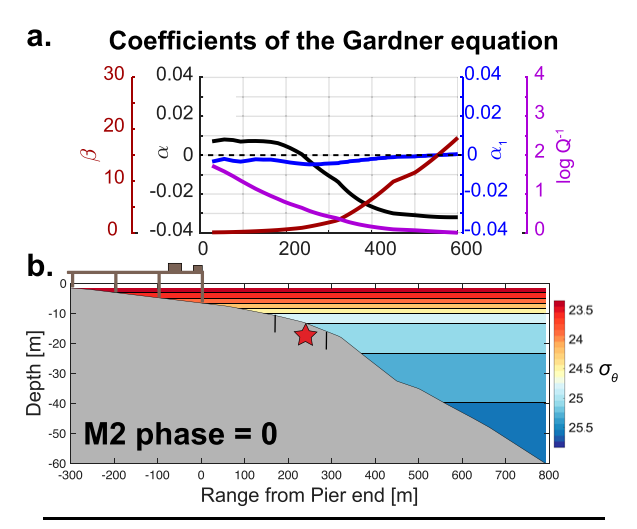
FIG. 3. (a) A 24-h record of DTS temperature measurements. The cyclic onshore–offshore motion of the internal tide and the tidal sharpening and broadening of the thermocline on the seafloor are indicated with arrows. A train of high-frequency nonlinear internal waves riding the crest of the internal tide is indicated with a black star. (b) 6-h mooring measurements of cross-shore velocity (color map, positive velocities are onshore) and isotherm displacement (solid lines). (c) Cross-shore velocity. The time range in (c) and (d) are indicated with a gray box in (b). (d) The vertical velocities associated with the passing train of NLIW waves shown in (c).

Kortenweg–de Vries (KdV) and extended-KdV frameworks was not met. So, following Lamb and Xiao (2014), we used the time-resolved stratification measured by the Wirewalker mooring to estimate the parameters of the variable coefficient Gardner Equation as a function of cross-shore position over a tidal cycle (appendix B). The Gardner formulation extends the weakly nonlinear analysis to a sloped domain, and reduces to the extended-KdV solution for flat bottoms.

The tidal variability of cross-shore position of the polarity reversal of the nonlinear parameter α is shown in Figs. 4a and 4c, corresponding to the internal-tide-driven change in the depth and shape of the thermocline (Figs. 4b,c). NLIWs of elevation can be expected inshore of this transition, which varied in cross-shore position by over 200 m over the canonical tidal cycle (Fig. 4).

The DTS observations substantiated the significance of this pattern. For example, there was a marked tidal cycle of several hundred meters in the offshore location of first appearance of the cold surges in Fig. 3a, suggesting that these depths/cross-shore ranges might be considered a subsurface analog of the shore-line intertidal zone. Similarly, vertical mooring observations at the 18-m isobath in 2014 indicated that the vertical structure of these shoaling waves transitioned from warm-core solitons of depression to cold-core solitons of elevation as the thermocline deepened on a tidal time scale (Figs. 3b-d).

The long-wave speed $c_{\rm Gardner}$ at the location of $\alpha=0$ values was estimated as $0.19\pm0.05~{\rm m~s}^{-1}$ when averaged over the tidal cycle, and demonstrated the tendency for the long-wave speed to decrease in shallow water. The half-width of the modeled soliton of depression was $\sim 50-60~{\rm m}$. From the inviscid perspective of the weakly nonlinear model, the slowing of the wave speed in shallow water implied an increase in wave amplitude required by the conservation of pressure–velocity energy flux. This yielded an amplification factor (1/Q) relative to



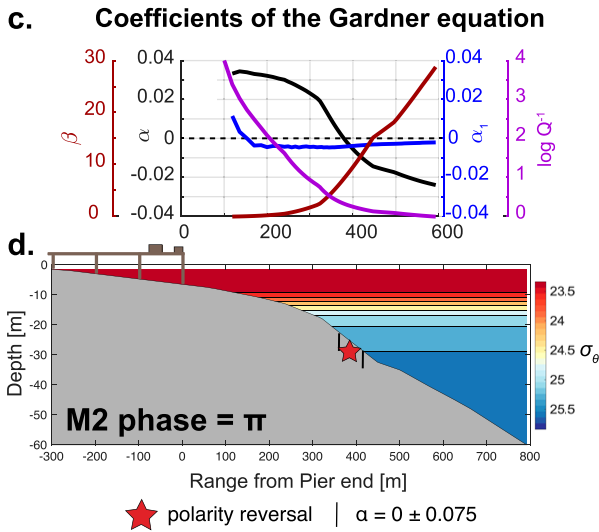


FIG. 4. (a),(c) Parameters of the variable coefficient Gardner equation $(\alpha, \alpha_1, \beta, Q)$ calculated as a function of cross-shore position for different phases of the M2 internal tide cycle. (b),(d) The stratification used as input to the analysis is shown for opposite phases of the semidiurnal internal tide.

the offshore edge of the experimental domain. Figures 4a and 4c show that 1/Q increased rapidly inshore of the transition to $\alpha > 0$.

c. The seabed expression of shoaling nonlinear internal waves of elevation

Distinct bands of cold water on the seabed could be tracked coherently for hundreds of meters in the cross-shore direction by the DTS, from their appearance at midshelf (~35-m depth) until their disappearance in the shallow water of the inner shelf, typically in ~10-m depth (Figs. 3a and 5). Each cold surge had a cross-shore width of 10–30 m and appeared concurrently with 80–100-m spacing on the cross-shore fiber (Figs. 5 and 6). The shoaling process from first appearance of a surge to its inshore dissipation generally took about 20–30 min.

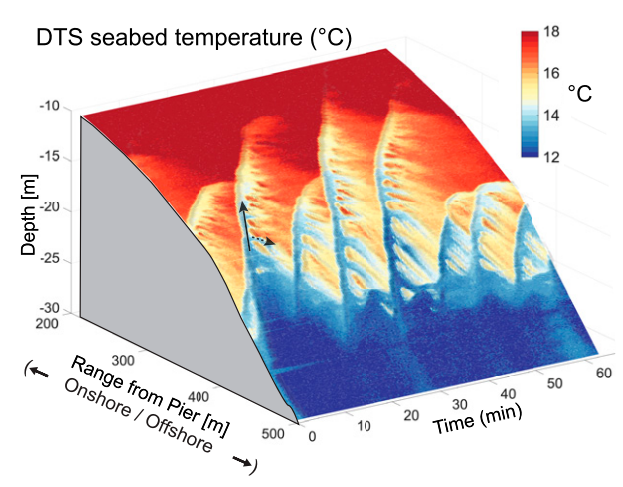


FIG. 5. A 60-min record of seabed temperature variability in depth (10–30 m), range from SIO Pier (200–500 m), and time from the fiber optic DTS system highlighting the arrival of a trains of NLIWs. Onshore surges of cold water were tracked continuously over the seafloor for hundreds of meters and tens of minutes (solid arrow). These surges were trailed by delicate disturbances in their wake, which appeared to move offshore (dotted arrow).

At times, the thermal stratification was such that the mean depth of the thermocline was approximately the same as the depth of the shore-parallel alongshore leg of the fiber optic array (22-m depth; dotted line in Fig. 1a). During these periods, the cold footprint of the shoaling surges could simultaneously be tracked in the cross-shore and alongshore directions (at a fixed cross-shore range). One such period is displayed in Fig. 6.

The observations indicated that the shoaling surges were coherent in the alongshore dimension over ranges up to 1 km, and crossed the alongshore portion of the fiber at the north end first, implying a southward component to their propagation direction (Figs. 6a,b). A rough approximation of the initial angle of approach for these waves was estimated assuming that the wavefront was straight, and comparing the simultaneous cross-shore and alongshore wavefront position in the region near the cable turn. This analysis suggested that the long-crested, narrow cold surges appeared to be rotated clockwise to the bathymetry, when viewed from above, by $\sim \! 10^{\circ}$ for the few examples captured.

The possibility that these long-crested cold surges on the seafloor DTS measurements were the signature of shoaling trains of NLIWs of elevation was suggested from both the analysis of the stratification and the measurements of the 2014 mooring array. To provide a comparison in terms of wave amplitude from the DTS seabed measurements, an estimate of the vertical displacement necessary to account for the measured temperature drop can be made as the equivalent to a upward disturbance of a mean "undisturbed" vertical temperature gradient (i.e., $\eta = [\langle T(z) \rangle - T(z,t)]/\langle dT/dz \rangle$, where brackets $\langle \ \rangle$ indicate a time average of the vertical temperature gradient observed by the DTS before arrival of the wave packets). By this measure, the DTS-tracked surges had

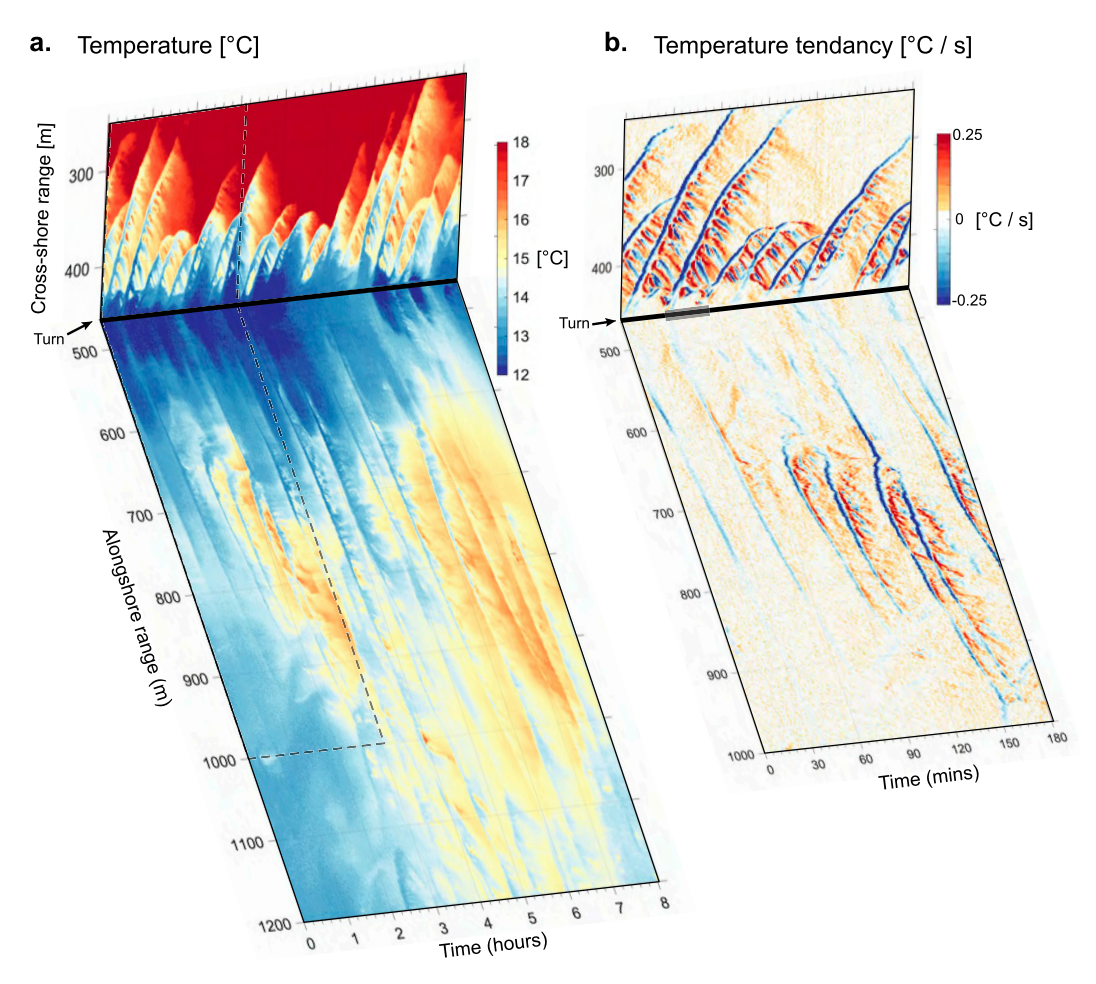


FIG. 6. The L-shaped alongshore DTS fiber array (dotted line in Fig. 1a) documented both along- and across-shore temperature variability. (a) DTS seabed temperature is shown against range for both the cross-shore and alongshore legs of the fiber array. The location of the turn is indicated in the figure as a discontinuity in the figure range axis. (b) A close-up view of the rate of temperature change in time against range and time. This map was used to estimate the azimuth, velocity, and dimensions of each shoaling wave. The gray bar in (b) shows the individual wave and wake studied in Fig. 9.

amplitudes on the order of several meters, agreeing with the wave displacements seen on the thermistor mooring in 2014 (Fig. 3b).

A further point of comparison can be gained by the continuous tracking of coherent surges across the inner shelf on the DTS array. Using an ad hoc cutoff value -0.0075° C s⁻¹, surges were identified as a coherent signature of a rapid drop in temperature propagating in range along the fiber (e.g., as in Fig. 6b). Once a feature was identified in this manner, 10 positions (in time and space) were collected for each of the individual surges that we tracked (n = 84). A second-order fit to the space-time coordinates of each wavefront provided initial propagation speed and deceleration rates. The estimated initial wave speeds ($c_0 = 0.14 \pm 0.04 \text{ m s}^{-1}$) and deceleration rates $(-4 \pm 2.5 \times 10^{-5} \text{ m s}^{-2})$ were distributed normally (n = 84). The wave speed estimates were qualitatively consistent with the predictions of the Gardner equation analysis (e.g., $c_{Gardner} = 0.15 \text{ m s}^{-1}$ at $\alpha = 0$ for the stratification shown in Fig. 4b).

4. Discussion

The observations documented that trains of NLIWs evolved into waves of elevation during shoaling, which is consistent with previous investigation of continental shelf internal waves from observations, theory and numerical simulation (Vlasenko and Hutter 2002; Grimshaw et al. 2004; D'Asaro et al. 2007; Shroyer et al. 2009; Hamann et al. 2018; Jones et al. 2020). Yet the spatially continuous DTS observations also showed that the signatures of the wave trains grew weaker and ultimately disappeared as the waves moved across the inner shelf toward the surfzone (Figs. 2b and 5). How much about the final stages of NLIW evolution in shallow water can be learned from the seabed temperature measurements alone?

a. Inshore of the polarity transition point I: Entrainment of upslope waters into the wave core

A key clue to the dynamics of the shoaling NLIWs was provided by the observation of continuous wave-core warming during the shoaling process (Fig. 7). Preliminary calculations suggested that this warming was too rapid to be associated with a turbulent diffusive exchange with warmer waters above the wave core, requiring an unrealistically large vertical diffusivity of $O(10^{-2})$ m² s⁻¹ (not shown). However, if the water in wave core was not trapped, warmer upslope water would be continuously ingested into the advancing wave, mixed with the water in the existing core, and eventually exhausted out of the trailing edge: a propagating, spatially confined mixing process.

In a frame of reference moving at the wave propagation speed over the course of a run-up event, both the wave-core temperature (defined as the 2-m range-averaged temperature centered 5 m offshore of the propagating wavefront) and the "entraining ambient" temperature (defined as the 2-m range-averaged temperature centered 5 m shoreward of the propagating wavefront) were quantified for 15 shoaling NLIWs of elevation. This yielded 1) an estimate of the rate of change of the wave-core temperature in time $(\partial T/\partial t)$ throughout the shoaling process (Fig. 7b) and 2) an estimate of the ratio of temperature of the wave core to the temperature of the upslope ambient fluid as a function of normalized cross-shore run-up distance (Fig. 7c).

Figure 7b shows the increase in wave-core temperature over the lifetime of 15 individual NLIWs of elevation, which was on the order of several degrees over the ~20–25-min shoaling time scale (best fit $0.003^{\circ}\text{C s}^{-1}$). Put another way, the observations indicated that a ~10 m wide by ~5 m amplitude NLIW wave core—one-half the cross-sectional area of an Olympic-sized (50 m × 2 m) swimming pool—warmed by 1°C every 5.5 min during the shoaling process.

To interpret this rapid warming rate, we considered a simple model of a bore-like wave of elevation [similar to the "solibore" of Henyey and Hoering (1997)]. In this model, warmer upslope waters are continuously being entrained into the wave core, where they are assumed to mix instantly, causing the observed warming. The goal of the model was to provide an estimate of the wave Froude number given the observed seabed temperature changes.

Consider an initial, upslope near-seafloor layer with parameters h_i , T_i , and u_i for height, temperature, and offshore velocity, respectively (Fig. 7b). This initial layer is ingested into the wave core, with properties h_c , T_c , u_c , and L_c , where L_c is the width of the core in the direction of propagation, and the other variables are as before. In a frame moving upslope with the core at speed c, all fluid velocities are offshore.

To conserve mass in this moving frame of reference (Fig. 7a)

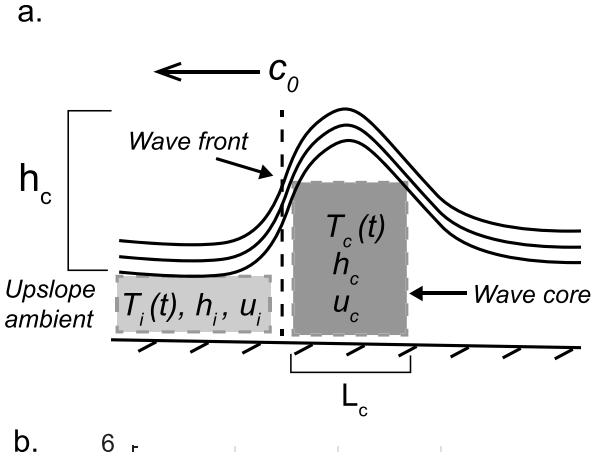
$$h_i(c + u_i) = h_c(c - u_c).$$
 (1)

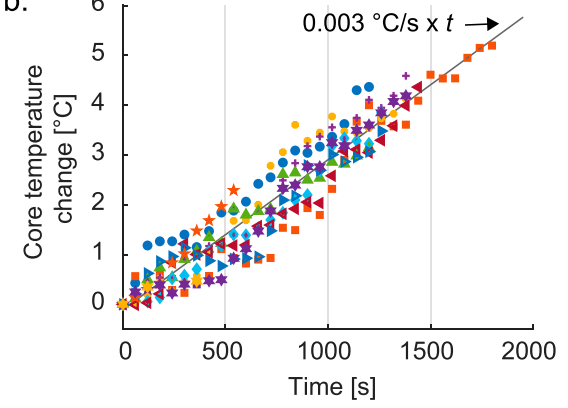
Using Fr = u_c/c , Eq. (1) becomes

$$h_i \left(1 + \frac{u_i}{u_c} \operatorname{Fr} \right) = h_c (1 - \operatorname{Fr}). \tag{2}$$

To conserve temperature in the NLIW core,

$$\frac{\partial T_c}{\partial t} = (T_i - T_c) \frac{h_i}{h_c L_c} (c + u_i). \tag{3}$$





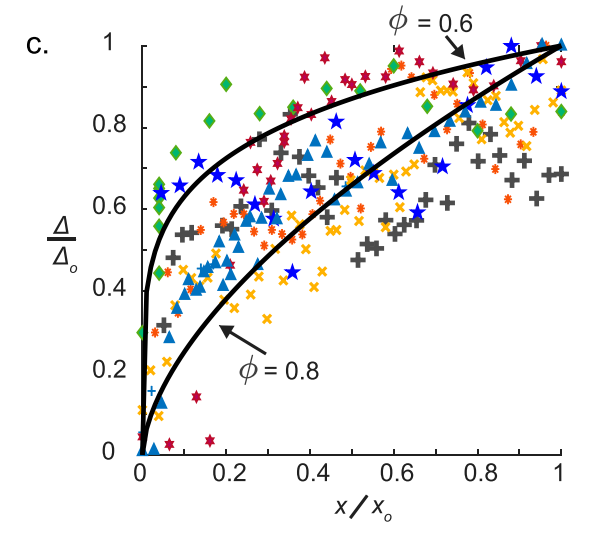


FIG. 7. (a) Schematic shoaling bore-like NLIW. (b) The wave core temperature change as a function of time during the run-up of 15 individual NLIWs. (c) Comparison of the density excess between the wave core and the upslope ambient as a function of normalized run-up distance in comparison to the bolus model of Wallace and Wilkinson (1988). Symbols: normalized wave-core density anomaly as a function of a normalized run-up distance for the waves analyzed. Solid lines: the predictions based on $\Delta/\Delta_0 = (x/x_0)^{2\phi-1}$ for values of $\phi = 0.6$ and 0.8 (Wallace and Wilkinson 1988).

Using Eq. (2), Eq. (3) becomes

$$\frac{\partial T_c}{\partial t} = (T_i - T_c) \frac{c}{L_c} (1 - \text{Fr}). \tag{4}$$

Rearranging,

$$Fr = 1 - \frac{\partial T_c}{\partial t} \frac{L_c}{c} \frac{1}{T_i - T_c}.$$
 (5)

A representative difference between the wave-core temperature and the uphill ambient fluid $T_i - T_c$ is 2°C (Fig. 3b). Given an observed wave footprint of $L_c = 10$ m, wave velocity of c = 0.15 m s⁻¹, and wave-core temperature rate of change in time of 0.003°C s⁻¹), Eq. (5) yielded a NLIW Fr number of Fr ≈ 0.9 . As constructed, the Fr estimate was relatively insensitive to changes in the aspect ratio of the wave core. For example, a factor of 2 decrease in h_c/L_c was only associated with a 10% decrease in Fr, from 0.9 to 0.8. Sinnett et al. (2018) estimated NLIW Fr exceeding 0.7 in this same area.

As an alternate approach, we assessed the bolus model of Wallace and Wilkinson (1988) with the DTS measurements. From the time-evolving ratio of ambient to wave core temperature, a normalized "density excess" of the wave core relative to the upslope ambient fluid (Δ/Δ_o) was estimated from temperature assuming a constant salinity of 33.5 and compared to the normalized run-up distance for each shoaling wave [e.g., compare Wallace and Wilkinson (1988), their Fig. 17, to our Fig. 7c].

Comparison of the warming of the wave core relative to the upstream ambient showed that, for the individual waves analyzed, the rate of increase of the wave-core temperature as a function of time or run-up distance was consistent with the expectation for a highly nonlinear bore-like feature or a selfsimilar bolus ingesting upslope ambient fluid (Wallace and Wilkinson 1988). The assertion that a bolus maintains its geometry during its run-up stage is equivalent to the geometric assessment of wave-core warming presented above. Both models require energetic turbulent mixing between subthermocline waters transported upslope in the wave core and the warm upslope ambient fluid, meaning the these highly nonlinear internal waves were driving exchange over the course of their run-up process. The mixed fluid of an intermediate temperature was observed by the DTS array after the passage of the wave core (Figs. 5 and 6a).

b. Inshore of the polarity transition point II: The trailing wave wake

A surprising aspect of the DTS observations was the appearance of small-scale temperature oscillations originating at the trailing edge of individual shoaling NLIWs (dotted arrow in Fig. 5). These temperature structures must be related to the nonlinear shoaling process, and were observed behind hundreds of individual waves over the course of the 2-month experiment. Yet, to our knowledge, they have not been described previously from field observations.

Plotting the change in temperature in time dT/dt as a function of time and range along the cable emphasized the

coherent nature of these trailing temperature oscillations (e.g., 250–450-m ranges in Fig. 6b). Puzzlingly, the phase of the temperature oscillations appeared to move *offshore*, counter to the direction of the shoaling wavefront (dotted arrow in Fig. 5). For example, the phase of a wake oscillation that began on the trailing NLIW face could be tracked continuously in time for several minutes, while moving 20–30 m offshore. Since the generating NLIW was simultaneously moving onshore, the cross-shore separation between the trailing oscillation and wavefront approached 100 m in many cases. In fact, it was clear that the wake perturbations could persist until the subsequent NLIW in the train arrived (Fig. 6b).

At the same time as coherent wake oscillations moved downrange (offshore) on the cross-shore fiber optic cable, similarly coherent signals could be seen to move southward in time on the alongshore leg of the fiber array (e.g., 700–900-m ranges in Fig. 6b). The concurrent offshore and southward propagation we observed cannot be generated by an onshore propagating undular bore, since the trailing dispersive tail travels in the same direction as the leading wave in the bore. Likewise, bottom roughness is unlikely to be the cause, since the sandy seabed offshore of SIO Pier is well surveyed and does not have significant elevation variation on the 20–50-m cross-shore scale of the trailing temperature variability apparent in the cross-shore DTS data (Fig. 5).

Instead, we hypothesized that the wake signature in cross-shore temperature variability arose from the presence of *alongshore* structure in the shoaling NLIW of elevation that was advected perpendicular to the cross-shore fiber array. To test this hypothesis, we constructed a three-dimensional kinematic model composed of a Gaussian crest—corresponding to the cold temperature anomaly of a shoaling soliton of elevation—trailed by a sinusoidal along-crest oscillation (Fig. 8a). This waveform was then propagated shoreward at fixed speed and incidence angle relative to a simulated cross-shore seabed fiber cable, while a weak ambient alongshore current was added to advect the wave form parallel to a simulated alongshore cable (Fig. 8b).

Based on the DTS observations, the horizontal half-width of the Gaussian disturbance was set to 10 m (Fig. 1a), c_x to the observed initial wave speed of the onshore shoaling wave of elevation ($c_x = 0.15$ m s⁻¹, Fig. 3a), v to the estimated alongshore advective velocity (v = 0.05 m s⁻¹, estimated from Fig. 6b), and θ to 10° clockwise from shore normal (Fig. 6). By choosing these parameters based on the observations, the alongshore wavelength of the trailing oscillation was then the only free parameter for the kinematic model, and could be adjusted until the pattern sampled by the synthetic DTS array matched the pattern observed by the in situ array (Fig. 8c).

The synthetic fiber optic array view of the kinematic model showed how a fixed wave form of a primary wave of elevation in the cross-shore dimension trailed by an oscillation in the alongshore dimension could create a pattern that is consistent with the DTS data (cf. Fig. 6b to Fig. 8c). The transverse oscillations appeared to move offshore on the cross-shore cable because 1) the wavefront approached at an angle to the cable and 2) the wave form was subject to weak alongshore advection. That is, the cross-shore DTS measurement was detecting

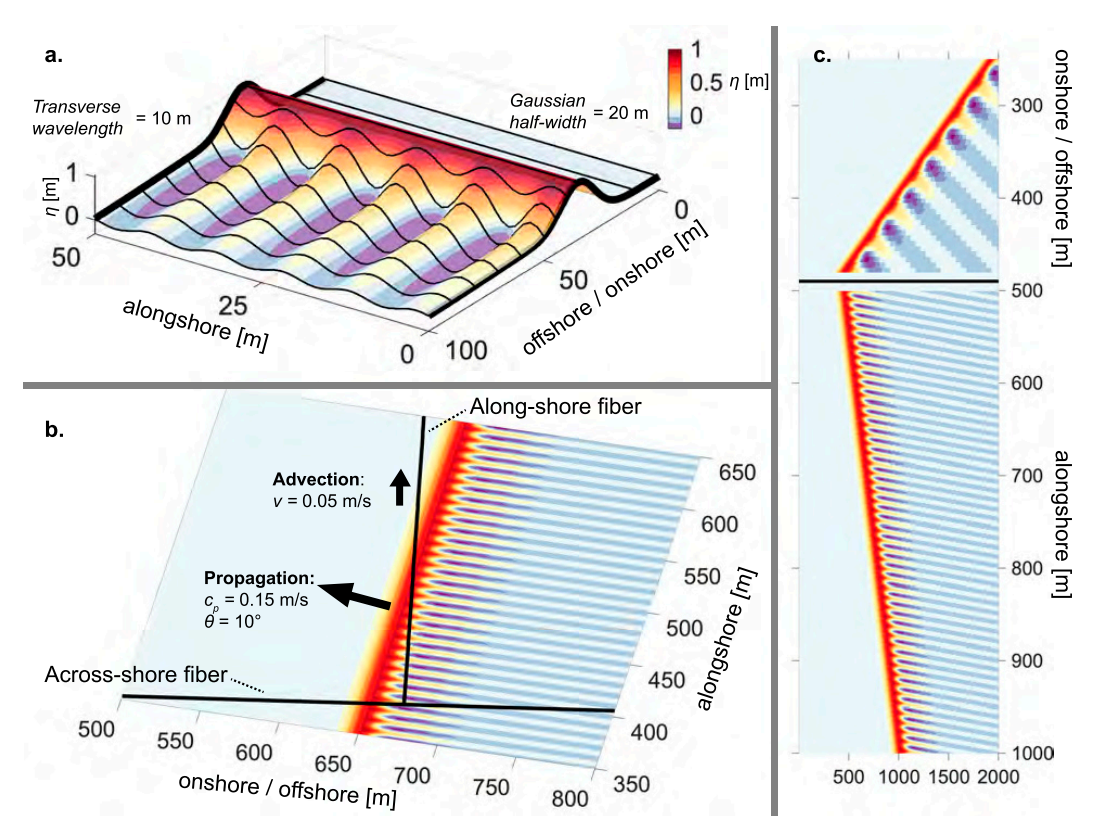


FIG. 8. (a)—(c) A kinematic simulator was used to generate a synthetic time—space maps of an onshore-propagating upward disturbance of the pycnocline, with a trailing wake of transverse oscillations. Panel (a) shows the simple waveform used in the simulation. The 2D waveform was then propagated and advected as indicated in (b), and then sampled as from a fixed L-shaped fiber [cf. (c) to Fig. 6]. The parameters for this kinematic model—azimuth, wave speed, alongshore current—were drawn from the DTS observations.

along-crest wave variability due to the presence of a weak, background alongshore drift of the pattern across the sensing cable.

This model permits reinterpretation of the cross-shore DTS observations as a scanning line sensor for alongshore variability. Assuming that the wake is approximately steady, a spacefor-time coordinate system transformation in analogy to Taylor's frozen field hypothesis can be applied to the DTS data. The frame of reference used for the transform was propagating at the initial cross-shore speed of the shoaling NLIW, and advecting in the alongshore dimension with a constant background current. This coordinate system rotation is equivalent an affine projection of the DTS basis coordinate system (appendix C; Horn and Woodham 1978). Since the temperature measurements provided an estimate of vertical amplitude as described above, a cross-shore range- and time-image of seabed temperature from the DTS can be converted into a synthetic aperture image of the wave form in terms of the cross-crest (x_{wave}) , along-crest (y_{wave}) , and displacement (η) scales (Fig. 9 and appendix C).

The along-crest (approximately alongshore) wavelength of the trailing wave wake was estimated as ~10 m, approximately 20% of the intercrest distance of the soliton train, and roughly equivalent to the cross-crest footprint of the shoaling NLIW.

These wakes were seen to extend away from the trailing edge of the NLIWs for distances of more than 50 m, and hint at alongshore alignment between successive wave crests (Fig. 9b). The estimated amplitudes of the wave of elevation ($\eta = \sim 5$ m) and the transverse oscillation were similar in magnitude. The steplike shape of the onshore surge can be seen in the leading edge of the projection (dark line in Fig. 9). Since the NLIWs were observed to have along-crest scales of a kilometer or more (Fig. 6), individual waves may have been trailed by dozens of transverse oscillations as they crossed the inner shelf.

5. Context and conclusions

Synthesizing previous research with the observations presented here, a picture emerges for the waters offshore of Scripps Beach. The energetic impinging internal tide was strongly modified by interaction with the steep local bathymetry, and much of the tidal energy was reflected back offshore (Fig. 2). However, in the process of this imperfect reflection, some of the forward-transmitted tidal energy was scattered into trains of long-crested NLIWs, which initially were well described by weakly nonlinear theory given the local timevarying stratification (Figs. 3–6). Unlike the internal tide, the temperature variance at periods of tens of minutes and

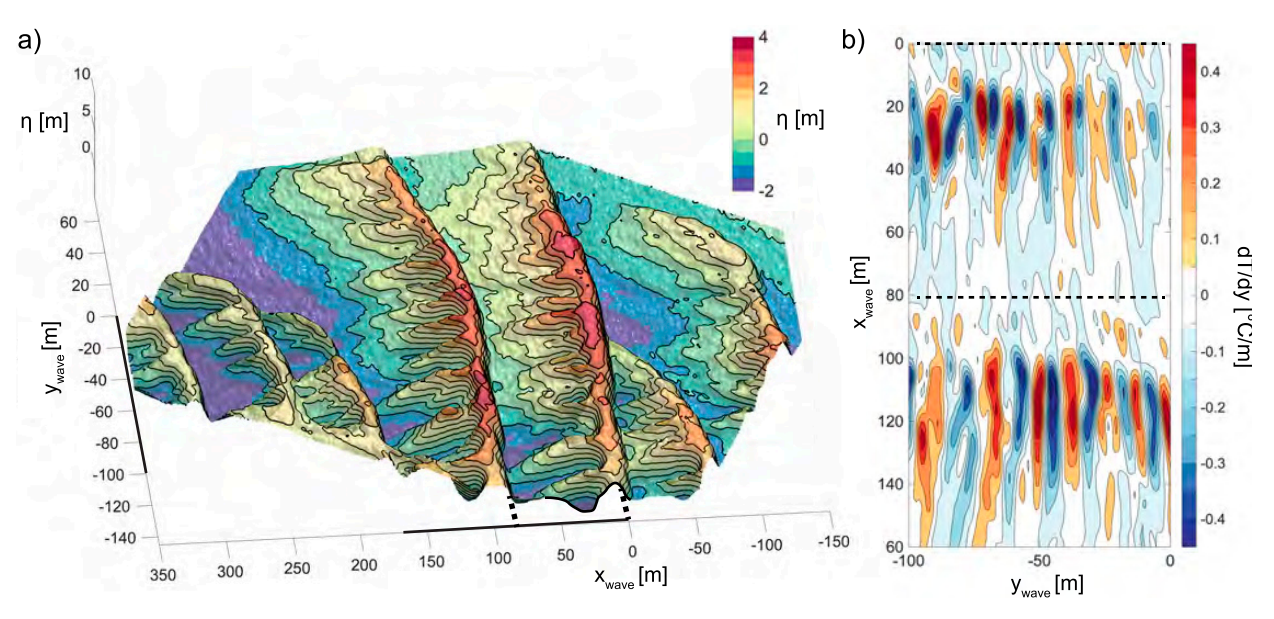


FIG. 9. (a) Using the wave speed, azimuth, and alongshore velocity estimated from the DTS array and the vertical mean and vertical temperature gradient from the Wirewalker profiles, the seafloor temperature observations in cross-shore distance and time were transformed to produce a cross- (x_{wave}) and along-crest (y_{wave}) spatial map of displacement $(\eta; m)$ that is translating at the shoaling wave speed. (b) After this fused data-model transformation is implemented, the wake disturbances—illustrated by the spatial gradient of temperature (dT/dy) in the close-up—appeared as narrow, parallel structures in the along-crest dimension. The transverse wave wake had an along-crest scale of ~ 10 m, and hinted at alignment between subsequent crests in the shoaling train. The dashed lines in both panels indicate the approximate location of the wave crests.

wavelengths of 100 m and less was almost entirely onshore polarized (Fig. 2b), suggesting that the trains of nonlinear internal waves we observed dissipated over the inner shelf. This statistical analysis was supported the individual NLIW tracking afforded by the seafloor DTS array, which showed that the seabed signature of the shoaling NLIWs gradually diminished and ultimately disappeared over the course of the shoaling process.

Geometrical arguments constrained by the DTS measurements indicated that the waves were strongly nonlinear (Fr ~ 0.9) and entrained upslope waters into their core, thereby mediating exchange between waters below the thermocline and those above. Further, this strongly nonlinear shoaling process led individual NLIWs to develop a coherent transverse wake, indicating that wave evolution during shoaling in shallow water was three dimensional and small scale.

How and where energy from the shoaling NLIWs in the coastal ocean is lost is of critical importance. The slope of the bathymetry, the vertical stratification, the background velocity shear and wave amplitude all impact internal wave shoaling and breaking (Venayagamoorthy and Fringer 2007; Aghsaee et al. 2010). Two-dimensional DNS solutions generate instabilities within the bottom boundary layer under the crest of a wave of elevation when a sheared background flow counter to the direction of wave propagation is present (Stastna and Lamb 2002; Diamessis and Redekopp 2006; Carr and Davies 2010). Shoaling enhances these instabilities and, for a sufficiently energetic wave on steep enough topography, two-dimensional wave breaking occurs (Aghsaee et al. 2010). In a more field-realistic parameter space, Xu and Stastna

(2020) showed that a train of waves of elevation generated by a fissioning process over a gentle slope developed a separation bubble, the breakdown of which yielded cross-boundary layer transport of similar efficiency as wave breaking over steeper slopes.

Three-dimensional DNS solutions emphasize that the development of vortical coherent structures is an important component of the shoaling process. These structures are typically aligned perpendicular to the direction of wave propagation, and arise from lobe and cleft instability at the forward wave face or shear instability in the trailing wave face (Gayen and Sarkar 2011; Arthur and Fringer 2014; Xu et al. 2016). The vertical shear in the wave-induced horizontal flow orchestrates the alignment of the vortical wake, leading to the formation of vortices with a major axis oriented perpendicular to the propagating wavefront (Arthur and Fringer 2014; Xu et al. 2016). For a bolus-like feature, vortical circulations are critical to the energetics during shoaling. Arthur and Fringer (2014) show that the mixing efficiency—the fraction of dissipation that alters the available potential energy of the fluid-is increased by the development of coherent structures, pointing to their likely importance for the exchanges in the coastal ocean. Similarly, Xu et al. (2016) demonstrated that the shear stress in the bottom boundary layer is enhanced by vortical coherent structures, suggesting that these dynamics may play an important role in sediment resuspension.

In an ongoing numerical study of shoaling nonlinear waves of elevation (A. Soloviev 2021, personal communication), trailing vortical structures had peak helicities $H \equiv \omega \times u_c \approx \pm 0.01$ m s⁻², where ω is the component of wake vorticity

parallel to the direction of propagation. If these helicities were occurring in the transverse wakes observed here, the rotational velocities would be of order 0.1 m s⁻¹, with the implication that the kinetic energy of the wake structure was not small compared to that of the generating waves. If so, the instability responsible for generating these transverse structures likely played a role in the energetics of shoaling NLIWs, perhaps to the point of limiting the potential of these waves to steepen and break via overturning.

The affine-transformed DTS observations hint that the transverse vortices do not just trail behind NLIW crests but perhaps extend coherently from crest to crest (Figs. 1a, 6b, and 9). An idealization that would explain this observation is one in which the entire shoaling wave train—or "internal tidal bore" (e.g., D'Asaro et al. 2007)—is a coherent structure of multiple crests with an associated transverse grid of vortical structures. As the pattern propagates shoreward, the transverse vortex structure would be axially stretched immediately following passage of a NLIW crest and compressed in advance of the subsequent crest. This rhythmic modulation of the transverse wake vortex street on the scale of the wave train might play a key role in energy exchange between the NLIW train and the stratified coastal ocean.

Quantifying the transformation of shoaling nonlinear internal waves in the ocean remains at the cutting edge of our observational capacity. The measurements presented here suggest that the process is inherently three dimensional. Future observations combining DTS arrays with multiple cables and more complex antennas designed to leverage the advection of fluid structures, along with direct measurements of velocity, turbulence, and dye dispersion, can address some of the uncertainties in the present work. Coordinating observations with numerical simulations is critical to the improved understanding of these dynamics. Given the demonstrated importance of internal wave shoaling and breaking to coastal sediment transport, pollutant dispersal, and ecosystem processes, it is likely such efforts would yield an improved capacity to predict the physical and biogeochemical state of the coastal ocean.

Acknowledgments. AJL gratefully acknowledges the support of the ONR Young Investigator Program fellowship (ONR N00014-17-1-2987) in completing this work. Drafts of this manuscript were improved by discussion with Jennifer MacKinnon and Matthew Alford. Jonathan Ladner, San Nguyen, Tyler Hughen, and Rich Walsh assisted in the field operations. Prof. John Selker and the Oregon State University Center for Transformative Environmental Monitoring Programs (CTEMPS) provided the Silixa Ultima DTS system. Simulations run by Alexander Soloviev provided insight into the vortical wake problem. Finally, the careful reviews and concrete suggestions graciously provided by three anonymous referees improved the final manuscript.

Data availability statement. The data presented here are available upon request.

APPENDIX A

Distributed Temperature Sensing Measurements

a. Fiber optic DTS principles of operation

The DTS is a remote measurement system that uses a point source laser to determine the range-resolved temperature along a fiber optic cable. The backscattered light has a broadband frequency content relative to the transmitted light, with spectral peaks at the transmitted frequency, the Stokes band (lower frequency than the transmitted pulse), and the anti-Stokes band (higher frequency than the transmitted pulse). The Stokes and anti-Stokes bands arise from the inelastic scattering of incident photons on molecules in the fiber, and the ratio in energy between the two bands is temperature dependent.

The DTS system uses range-gated returns from a pulsed near-infrared laser to determine the ratio of energy in the Stokes versus anti-Stokes bands against distance, and thus infer the temperature at continuous ranges along a fiber optic cable. These measurements can be collected at a sub-1-m resolution, a temporal sampling of ~1 s continuously over kilometers. Our experiments with systems in 2012 in comparison to those tested in 2004 showed that the sensing systems had matured to the point where oceanographic observations with the DTS were possible. DTS technology has a proven track record in groundwater, streamflow, atmospheric boundary layer, and underice applications. A methodology to calibrate the DTS system for oceanographic uses was recently published (Sinnett et al. 2020). That study was also conducted from SIO Pier, using the same fiber optic cable and Silixa Ultima SE DTS system as the earlier observations reported here.

b. 2013 fiber optic DTS measurements

The 2013 DTS experiment was carried out from 25 June to 23 August 2013. A Silixa Inc. ULTIMA DTS system, provided by Oregon State University Center for Transformative Environmental Monitoring Programs (CTEMPs; https://ctemps.org/), was installed on the end of SIO pier. The DTS is a roughly desktop computer-sized instrument that runs on shore power and consumes 75 W continuously. The ULTIMA DTS was configured to record temperature along two fiber optic cables laid on the seafloor every 20 s with 60-cm along-cable spatial resolution. The Optical Fiber Solutions mini LT Flat Drop jacketed and fiberglass reinforced cables ran from the DTS system through a calibration bath (composed of 20 m of coiled fiber in an Igloo cooler) and then were dropped from the pier end to an awaiting small boat. The "cross-shore" cable was pulled approximately 900 m at a bearing of 285° (essentially across-isobath). Divers affixed the fiber to the base of the northern, offshore-most pier piling, and also to a sand anchor at approximately 22-m depth, 450 m from the pier. A SBE-56 thermistor was affixed to the sand anchor. The terminus of the cable was anchored approximately 900 m from the end of the pier in 85-m depth with a 15-pound Danforth anchor and 5 m of chain. A SBE-37 pressure-

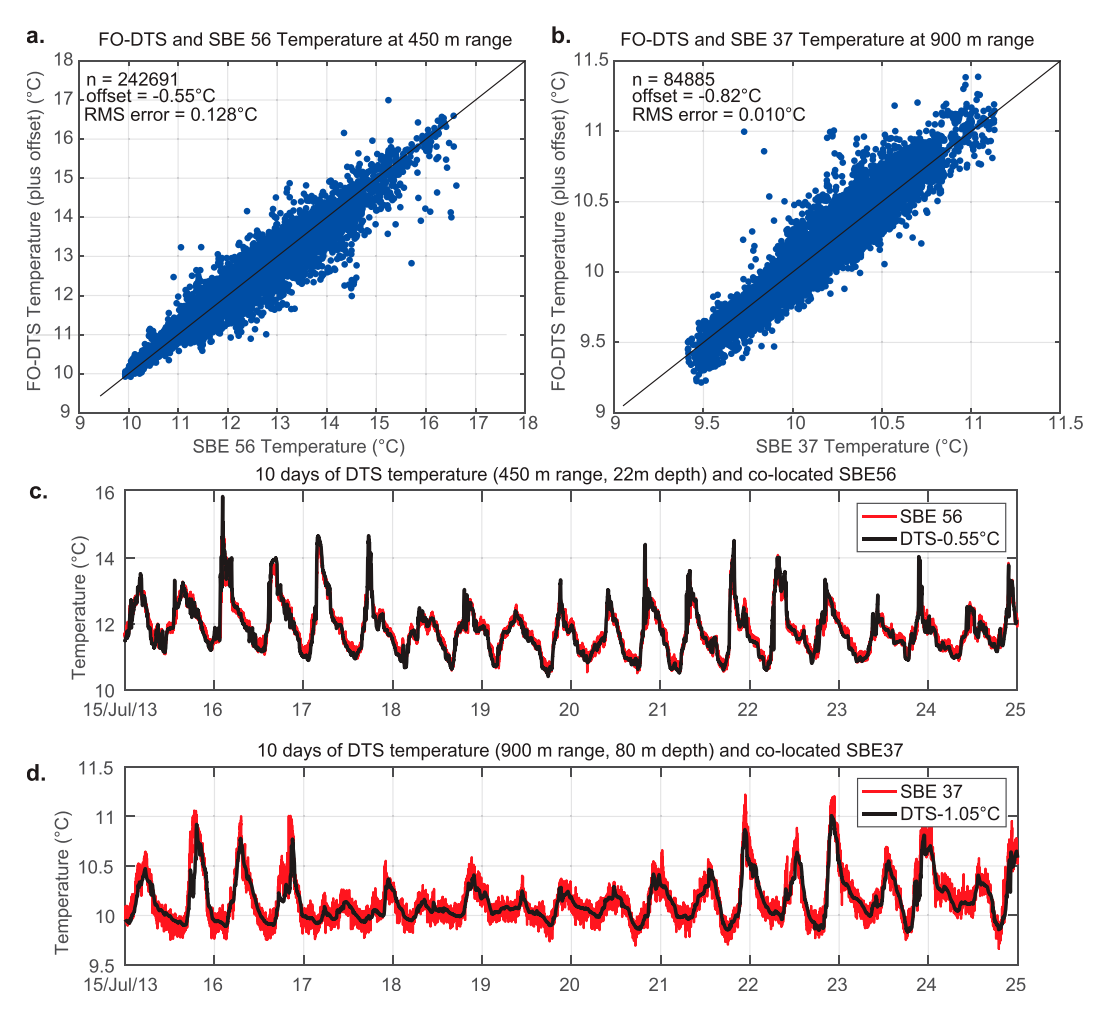


FIG. A1. Characterization of the fidelity of DTS measurements. Sea-Bird Instruments (SBE) thermistors were collocated with the DTS cable at 450-m range (SBE 56, ~22-m depth) and 900-m range (SBE 37, ~80-m depth). (a),(b) The observations were used to calculate temperature offset and estimate a time-dependent RMS error of the DTS observations. Time series of calibrated temperature for a selected 10-day period is shown for the (c) inshore and (d) offshore instrument locations.

temperature sensor was deployed with the offshore anchor and cable terminus. The second, L-shaped fiber was laid parallel to the cross-shore fiber until the 22-m depth sand anchor, and then pulled southward for 1 km. The GPS position of the deployment vessel was recorded while the cable was laid, allowing the fiber location to be determined. Local multibeam bathymetry was used to map the fiber position to depth below datum.

We configured the SBE-56 temperature sensor to sample at 5-s intervals at a nominal 450m range along the fiber in a tidally averaged 22-m water depth. The SBE-37 pressure-temperature recorder was configured to sample at 3-min intervals, at a tidally averaged depth of 85 m, near the terminus of the cable (approximately 850 m from the SIO pier). These point measurements were collected over the ~2-month duration of the experiment (Fig. A1).

Silixa Inc. specifications indicated a precision of $\sim\!0.1^{\circ}\mathrm{C}$ at 500-m range at a spatiotemporal sampling resolution (0.6 m

by ~ 20 s), and a $\sim 0.01^{\circ}$ C precision at 1 km with a 3-min average over a 2-m along-cable average. To test the precision of the DTS measurements, we compared them with to the SBE thermistors deployed over the length of the deployment. The thermistors were used to determine a deployment-mean offset between fiber range and temperature, and to estimate the root-mean-square error between the thermistors and nearest range fiber observation (Fig. A1).

The point observations confirmed the broad fidelity of the DTS observations. The DTS temperature offset was -0.82° C at 850-m range and -0.55° C at 450-m range. As the DTS system autocalibrates relative to the ice bath, we assumed a 0°C offset at the pier end. The resulting discrepancy was estimated linearly as at -0.001° C per meter, and this gradient was applied to the DTS time series. The environmental temperature gradients associated with wave shoaling were at least two orders of magnitude larger than this calibration

gradient. The calculated offset and attenuation were similar to the estimate by Sinnett et al. (2020).

The root-mean-square (RMS) error of the DTS temperature relative to the SBE thermistor measurements was 0.01° C over a 2-m spatial and 3-min temporal averaging at the terminus of the cable (range = 950 m; $n = 84\,885$) and 0.1° C at 0.6-m spatial and 0.3-min temporal averaging at 450-m range ($n = 242\,691$). Although relatively coarse by oceanographic standards, these precisions were sufficient to elucidate the spatiotemporal variability in bottom temperature in this strongly vertically stratified system.

APPENDIX B

Estimating the Terms of the Gardner Equation

Weakly nonlinear internal waves have been studied in nondissipative spatially homogenous environments using the Korteweg de Vries and extended Korteweg de Vries family of equations (Grimshaw et al. 2004; Helfrich and Melville 2006; Shroyer et al. 2009, 2011). In shoaling situations, KdV-type equations are extended through an additional term to conserve the pressure–velocity energy flux to first order (Lamb and Xiao 2014).

The resulting Gardner family of equations:

$$\frac{\partial \eta}{\partial t} + c_o + \alpha(x)\eta \frac{\partial \eta}{\partial x} + \alpha_1(x)\eta^2 \frac{\partial \eta}{\partial x} + \beta(x)\frac{\partial^3 \eta}{\partial x^3} + \frac{c_o}{2} \frac{\eta}{Q} \frac{\partial Q}{\partial x} = 0$$
(B1)

generally produce dispersion where an initial disturbance sheds a trail of more slowly moving waves as it propagates upslope (Lamb and Xiao 2014).

Here, η is the vertical displacement of the pycnocline, x and t indicate horizontal space and time, respectively, and c_0 is the linear long-wave speed. The terms α and α_1 are the quadratic and cubic nonlinear parameters, respectively, and β is the dispersive parameter. These terms are also found in the extended-KdV formulation (Grimshaw et al. 2004; Helfrich and Melville 2006; Shroyer et al. 2011).

The final parameter Q is given by

$$Q = \frac{\int_{-H}^{0} c_o^3 \left(\frac{\partial \phi}{\partial z}\right)^2 dz}{\int_{-H_o}^{0} \left[c_o^3 \left(\frac{\partial \phi}{\partial z}\right)^2\right]_{Y_0} dz}$$
(B2)

and $Q(|_{x_0})$ is the incident, offshore value of Q, as discussed in Small (2001).

Previous observations documented how the baroclinic internal tide modulates the thermocline structure in the vicinity of Scripps Pier (e.g., Winant 1974; Alberty et al. 2017; Sinnett et al. 2018). To study how this modulation affects the nearshore waveguide, a canonical tidal cycle was synthesized from the Wirewalker profiler observations at the 50-m isobath (\sim 800 m from the pier end). To do so, we fit the Wirewalker observations of density $\rho(z, t)$ at the K1,

M2, 2M2, and 3M2 frequencies from a representative 3-day period (4–7 July 2013). The short length of the record used in this analysis was chosen to assure that the internal tide signal was stationary for the harmonic analysis (Nash et al. 2012). The harmonics of the fundamental semidiurnal tide were included in the fit given the finding of Alberty et al. (2017) that interaction with the steep bathymetry of the adjacent La Jolla Canyon generated energetic harmonics. The Wirewalker data spanned 2–45-m depth in 25-cm increments, with a profile every ~4 min (roughly 750 profiles were used in the analysis).

The fitted harmonic coefficients were used to create a 24-h, canonical time series of the internal tide driven modulation of the stratification at the Wirewalker mooring location. The isopycnal surfaces are assumed to be level across the inner shelf, allowing our harmonic analysis from the single mooring location to be used in the spatially dependent Gardner equation, as described below. Since the velocity field extracted from a similar harmonic analysis on the Wirewalker velocities was always <5 cm s⁻¹, we assume that the background shear flow was negligible.

The linear long-wave speed is estimated from the canonical stratification by solving an eigenvalue problem for a linear vertical structure function $\phi(z)$ at each cross-shore position in x and at each time t in the tidal cycle (Grimshaw et al. 2004; Shroyer et al. 2009), and then by applying a first-order correction to the eigenmode [Grimshaw et al. 2004, Eq. (6)]. The parameters α , α_1 , β , and Q follow from the linear long-wave speed.

APPENDIX C

Affine Transform of the DTS Observations

Given the hypothesis that the seabed temperature signature measured by the DTS is caused by 3D wave form of a shoaling, highly nonlinear wave of elevation trailing a transverse oscillation subject to weak alongshore advection, one can reinterpret the range-time DTS observations to form a synthetic aperture in the "unsampled" along-crest dimension from purely cross-shore measurements. This transformation reveals the spatial scale of the transverse instability as it exists in nature.

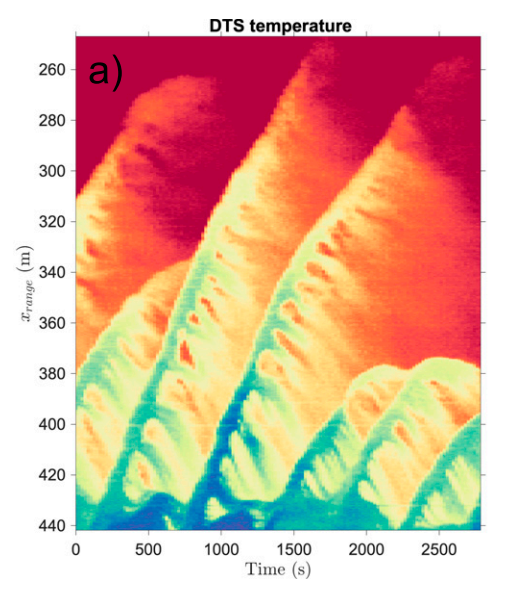
To do this, we transform the 2D basis of the data (Earth-referenced range along the fiber and time) to a frame of reference that is translating with the initial speed of the wave of elevation front in the x dimension c_x , and is advected in the alongshore direction by velocity v.

This is achieved by a coordinate transform of the temperature signal $T(t, x_{\text{range}})$ into a wave-following and advecting frame of reference $T(\dot{t}_{\text{wave}}, \dot{x}_{\text{wave}})$, where

$$\dot{x}_{\text{wave}} = x_{\text{range}} + [c_x \cos(\theta)]t$$
 (m) (C1)

$$\dot{t}_{\text{wave}} = t + \frac{x_{\text{range}}}{v \cos(\theta)}$$
 (c2)

and θ is the angle of propagation relative to the fiber optic cable. In this frame, signals propagating at the speed of the



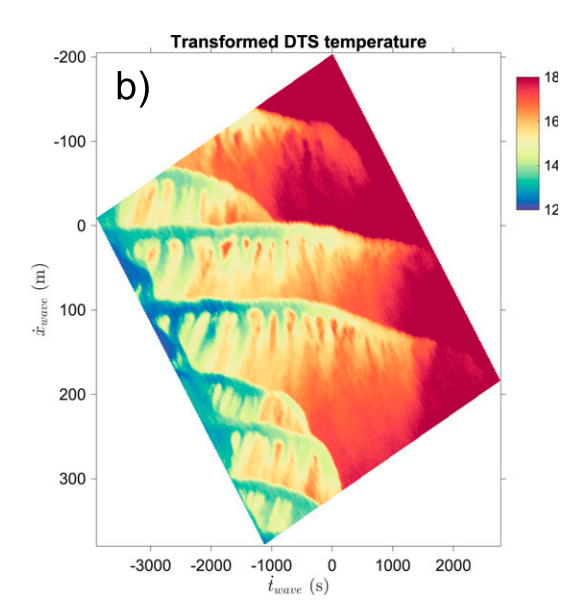


FIG. C1. (a) A range-time image of temperature from the fiber optic array. These data correspond with the highlighted portion of Fig. 6b in the main manuscript. (b) Affine transformed DTS observations. The y axis is (a) is transformed in a range (\dot{x}) relative a constant propagation speed of c_x of 0.15 m s⁻¹, while the x axis in (a) is backrotated (\dot{t}) by the alongshore advection velocity v of 0.05 m s⁻¹. These transformations yield the temperature perturbations projected the along- and across-crest coordinate system shown in Fig. 9.

wave appear at fixed \dot{x} , while the transformation in time acts to align the measurements as a function of time and range by $x_{\text{range}}/[v\cos(\theta)]$, accounting for the slow advection of the wave form by the alongshore current v.

Such a coordinate system transformation is equivalent to a two-dimensional affine shear transformation of the DTS observations, where the temperature measurement "pixels" are registered within a space-time "image." This type of transformation preserves the area of each pixel and preserves parallelism in the image (Horn and Woodham 1978), and is in broad use for correcting azimuth in satellite data.

It is implemented as

$$[\dot{t}_{\text{wave}} \ \dot{x}_{\text{wave}} \ 1] = [t \ x_{\text{range}} \ 1] \begin{bmatrix} 1 & c_x \cos(\theta) & 0\\ \frac{1}{v \cos(\theta)} & 1 & 0\\ 0 & 0 & 1 \end{bmatrix}$$

using the MATLAB Image processing toolbox (Fig. C1, Fig. 9).

The transformed time dimension i_{wave} can be then related to along-crest horizontal scale from time using the advection speed v and the approach angle θ as $\dot{y}_{\text{wave}} = [v\cos(\theta)]\dot{t}_{\text{wave}}$.

The result of this transformation yields several scales: the across-shore footprint of the wave of elevation (10–20 m in $\dot{x}_{\rm wave}$), the instantaneous across-shore separation of the waves of elevation (80–100 m in \dot{x}), and the alongshore wavelength of the transverse oscillations (~10 m in $\dot{y}_{\rm wave}$) (Figs. 9 and C1).

REFERENCES

Aghsaee, P., L. Boegman, and K. G. Lamb, 2010: Breaking of shoaling internal solitary waves. J. Fluid Mech., 659, 289–317, https://doi.org/10.1017/S002211201000248X.

Alberty, M. S., S. Billheimer, M. M. Hamann, C. Y. Ou, V. Tamsitt, A. J. Lucas, and M. H. Alford, 2017: A reflecting, steepening, and breaking internal tide in a submarine canyon. J. Geophys. Res. Oceans, 122, 6872–6882, https://doi.org/10.1002/2016JC012583.

Alford, M. H., and Coauthors, 2015: The formation and fate of internal waves in the South China Sea. *Nature*, **521**, 65–69, https://doi.org/10.1038/nature14399.

Arthur, R. S., and O. B. Fringer, 2014: The dynamics of breaking internal solitary waves on slopes. *J. Fluid Mech.*, **761**, 360–398, https://doi.org/10.1017/jfm.2014.641.

Becherer, J., J. N. Moum, J. A. Colosi, J. A. Lerczak, and J. M. McSweeney, 2020: Turbulence asymmetries in bottom boundary layer velocity pulses associated with onshore-propagating nonlinear internal waves. *J. Phys. Oceanogr.*, 50, 2373–2391, https://doi.org/10.1175/JPO-D-19-0178.1.

Bernal, L. P., and A. Roshko, 1986: Streamwise vortex structure in plane mixing layers. *J. Fluid Mech.*, **170**, 499–525, https://doi.org/10.1017/S002211208600099X.

Boegman, L., and M. Stastna, 2019: Sediment resuspension and transport by internal solitary waves. *Annu. Rev. Fluid Mech.*, 51, 129–154, https://doi.org/10.1146/annurev-fluid-122316-045049.

Bourgault, D., D. E. Kelley, and P. S. Galbraith, 2008: Turbulence and boluses on an internal beach. *J. Mar. Res.*, **66**, 563–588, https://doi.org/10.1357/002224008787536835.

—, M. Morsilli, C. Richards, U. Neumeier, and D. E. Kelley, 2014: Sediment resuspension and nepheloid layers induced by long internal solitary waves shoaling orthogonally on

- uniform slopes. *Cont. Shelf Res.*, **72**, 21–33, https://doi.org/10. 1016/j.csr.2013.10.019.
- Buijsman, M. C., Y. Uchiyama, J. C. McWilliams, and C. R. Hill-Lindsay, 2012: Modeling semidiurnal internal tide variability in the Southern California bight. *J. Phys. Oceanogr.*, 42, 62–77, https://doi.org/10.1175/2011JPO4597.1.
- Carr, M., and P. A. Davies, 2010: Boundary layer flow beneath an internal solitary wave of elevation. *Phys. Fluids*, 22, 026601, https://doi.org/10.1063/1.3327289.
- Colosi, J. A., N. Kumar, S. H. Suanda, T. M. Freismuth, and J. H. MacMahan, 2018: Statistics of internal tide bores and internal solitary waves observed on the inner continental shelf off point sal, California. J. Phys. Oceanogr., 48, 123–143, https://doi.org/10.1175/JPO-D-17-0045.1.
- Connolly, T. P., and A. R. Kirincich, 2019: High-resolution observations of subsurface fronts and alongshore bottom temperature variability over the inner shelf. *J. Geophys. Res. Oceans*, 124, 593–614, https://doi.org/10.1029/2018JC014454.
- D'Asaro, E., R. Lien, and F. Henyey, 2007: High-frequency internal waves on the oregon continental shelf. *J. Phys. Oceanogr.*, 37, 1956–1967, https://doi.org/10.1175/JPO3096.1.
- Davis, K. A., R. S. Arthur, E. C. Reid, J. S. Rogers, O. B. Fringer, T. M. DeCarlo, and A. L. Cohen, 2020: Fate of internal waves on a shallow shelf. *J. Geophys. Res. Oceans*, 125, e2019JC015377, https://doi.org/10.1029/2019JC015377.
- Diamessis, P. J., and L. G. Redekopp, 2006: Numerical investigation of solitary internal wave induced global instability in shallow water benthic boundary layers. *J. Phys. Oceanogr.*, 36, 784–812, https://doi.org/10.1175/JPO2900.1.
- Ewing, G. C., 1950: Relation between band slicks at the surface and internal waves in the sea. *Science*, **111**, 91–94, https://doi.org/10.1126/science.111.2874.91.b.
- Fritts, D. C., J. R. Isler, and Ø. Andreassen, 1994: Gravity wave breaking in two and three dimensions: 2. three-dimensional evolution and instability structure. *J. Geophys. Res.*, 99, 8109– 8123, https://doi.org/10.1029/93JD03436.
- Gayen, B., and S. Sarkar, 2011: Boundary mixing by density overturns in an internal tidal beam. *Geophys. Res. Lett.*, 38, L14608, https://doi.org/10.1029/2011GL048135.
- Grimshaw, R., E. Pelinovsky, T. Talipova, and A. Kurkin, 2004: Simulation of the transformation of internal solitary waves on oceanic shelves. *J. Phys. Oceanogr.*, **34**, 2774–2791, https://doi.org/10.1175/JPO2652.1.
- Hamann, M. M., M. H. Alford, and J. B. Mickett, 2018: Generation and propagation of nonlinear internal waves in sheared currents over the Washington Continental Shelf. J. Geophys. Res. Oceans, 123, 2381–2400, https://doi.org/10.1002/2017JC013388.
- —, —, A. J. Lucas, A. F. Waterhouse, and G. Voet, 2021: Turbulence driven by reflected internal tides in a supercritical submarine canyon. *J. Phys. Oceanogr.*, **51**, 591–609, https://doi.org/10.1175/JPO-D-20-0123.1.
- Helfrich, K. R., and W. K. Melville, 2006: Long nonlinear internal waves. *Annu. Rev. Fluid Mech.*, 38, 395–425, https://doi.org/ 10.1146/annurev.fluid.38.050304.092129.
- Henyey, F. S., and A. Hoering, 1997: Energetics of borelike internal waves. J. Geophys. Res., 102, 3323–3330, https://doi.org/10.1029/96JC03558.
- Horn, B., and R. Woodham, 1978: LANDSAT MSS coordinate transformations. A. I. Memo 465, Massachusetts Institute of Technology, 54 pp.

- Jackson, C. R., 2004: An atlas of oceanic internal solitary waves and their properties. 2nd ed., Office of Naval Research, 560 pp., http://www.internalwaveatlas.com/Atlas2_index.html.
- Johnston, T. S., and D. L. Rudnick, 2015: Trapped diurnal internal tides, propagating semidiurnal internal tides, and mixing estimates in the California Current system from sustained glider observations, 2006–2012. *Deep-Sea Res. II*, 112, 61–78, https:// doi.org/10.1016/j.dsr2.2014.03.009.
- Jones, N. L., G. N. Ivey, M. D. Rayson, and S.M. Kelly, 2020: Mixing driven by breaking nonlinear internal waves. *Geophys. Res. Lett.*, 47, e2020GL089591, https://doi.org/10.1029/2020GL089591.
- Klymak, J. M., and J. N. Moum, 2003: Internal solitary waves of elevation advancing on a shoaling shelf. *Geophys. Res. Lett.*, 30, 2045, https://doi.org/10.1029/2003GL017706.
- Lamb, K. G., 2014: Internal wave breaking and dissipation mechanisms on the continental slope/shelf. *Annu. Rev. Fluid Mech.*, 46, 231–254, https://doi.org/10.1146/annurev-fluid-011212-140701.
- —, and W. Xiao, 2014: Internal solitary waves shoaling onto a shelf: Comparisons of weakly-nonlinear and fully nonlinear models for hyperbolic-tangent stratifications. *Ocean Modell.*, 78, 17–34, https://doi.org/10.1016/j.ocemod.2014.02.005.
- Lasheras, J. C., and H. Choi, 1988: Three-dimensional instability of a plane free shear layer: An experimental study of the formation and evolution of streamwise vortices. *J. Fluid Mech.*, 189, 53–86, https://doi.org/10.1017/S0022112088000916.
- Lerczak, J. A., 2000: Internal waves on the southern California Shelf. Ph.D. thesis, Scripps Institution of Oceanography, University of California, San Diego, 244 pp.
- —, C. D. Winant, and M. C. Hendershott, 2003: Observations of the semidiurnal internal tide on the southern California slope and shelf. *J. Geophys. Res.*, 108, 3068, https://doi.org/10.1029/2001JC001128.
- Liu, A. K., Y. S. Chang, M.-K. Hsu, and N. K. Liang, 1998: Evolution of nonlinear internal waves in the East and South China Seas. *J. Geophys. Res.*, 103, 7995–8008, https://doi.org/10.1029/97JC01918.
- Lucas, A. J., P. Franks, and C. Dupont, 2011: Horizontal internaltide fluxes support elevated phytoplankton productivity over the inner continental shelf. *Limnol. Oceanogr. Fluids Envi*ron., 1, 56–74, https://doi.org/10.1215/21573698-1258185.
- —, R. Pinkel, and M. Alford, 2017: Ocean wave energy for long endurance, broad bandwidth ocean monitoring. *Ocean-ography*, 30, 126–127, https://doi.org/10.5670/oceanog.2017. 232.
- McPhee-Shaw, E. E., and E. Kunze, 2002: Boundary layer intrusions from a sloping bottom: A mechanism for generating intermediate nepheloid layers. *J. Geophys. Res.*, **107**, 3050, https://doi.org/10.1029/2001JC000801.
- McSweeney, J. M., and Coauthors, 2020: Observations of shoaling nonlinear internal bores across the central California inner shelf. J. Phys. Oceanogr., 50, 111–132, https://doi.org/10.1175/ JPO-D-19-0125.1.
- Nam, S., and U. Send, 2011: Direct evidence of deep water intrusions onto the continental shelf via surging internal tides. J. Geophys. Res., 116, C05004, https://doi.org/10.1029/2010JC006692.
- Nash, J. D., S. M. Kelly, E. L. Shroyer, J. N. Moum, and T. F. Duda, 2012: The unpredictable nature of internal tides on continental shelves. *J. Phys. Oceanogr.*, 42, 1981–2000, https://doi.org/10.1175/JPO-D-12-028.1.

- Pineda, J., 1999: Circulation and larval distribution in internal tidal bore warm fronts. *Limnol. Oceanogr.*, 44, 1400–1414, https://doi.org/10.4319/lo.1999.44.6.1400.
- Pinkel, R., M. A. Goldin, J. A. Smith, O. M. Sun, A. A. Aja, M. N. Bui, and T. Hughen, 2011: The wirewalker: A vertically profiling instrument carrier powered by ocean waves. *J. Atmos. Oceanic Technol.*, 28, 426–435, https://doi.org/10.1175/ 2010JTECHO805.1.
- Ponte, A. L., and B. Cornuelle, 2013: Coastal numerical modelling of tides: Sensitivity to domain size and remotely generated internal tide. *Ocean Modell.*, 62, 17–26, https://doi.org/10. 1016/j.ocemod.2012.11.007.
- Rainville, L., and R. Pinkel, 2001: Wirewalker: An autonomous wave-powered vertical profiler. J. Atmos. Oceanic Technol., 18, 1048–1051, https://doi.org/10.1175/1520-0426(2001)018<1048: WAAWPV>2.0.CO:2.
- Selker, J., N. van de Giesen, M. Westhoff, W. Luxemburg, and M. B. Parlange, 2006: Fiber optics opens window on stream dynamics. *Geophys. Res. Lett.*, 33, L24401, https://doi.org/10. 1029/2006GL027979.
- Sharples, J., and Coauthors, 2007: Spring-neap modulation of internal tide mixing and vertical nitrate fluxes at a shelf edge in summer. *Limnol. Oceanogr.*, 52, 1735–1747, https://doi.org/ 10.4319/lo.2007.52.5.1735.
- Shroyer, E. L., J. Moum, and J. Nash, 2009: Observations of polarity reversal in shoaling nonlinear internal waves. *J. Phys. Oceanogr.*, 39, 691–701, https://doi.org/10.1175/ 2008JPO3953.1.
- —, J. N. Moum, and J. D. Nash, 2010: Vertical heat flux and lateral mass transport in nonlinear internal waves. *Geophys. Res. Lett.*, 37, L08601, https://doi.org/10.1029/2010GL042715.
- Shroyer, E., J. Moum, and J. Nash, 2011: Nonlinear internal waves over New Jersey's continental shelf. *J. Geophys. Res.*, **116**, C03022, https://doi.org/10.1029/2010JC006332.
- Sinnett, G., F. Feddersen, A. J. Lucas, G. Pawlak, and E. Terrill, 2018: Observations of nonlinear internal wave run-up to the surfzone. *J. Phys. Oceanogr.*, 48, 531–554, https://doi.org/10. 1175/JPO-D-17-0210.1.
- —, K. A. Davis, and A. J. Lucas, 2020: Distributed temperature sensing for oceanographic applications. *J. Atmos. Oceanic Technol.*, 37, 1987–1997, https://doi.org/10.1175/JTECH-D-20-0066.1
- Small, J., 2001: A nonlinear model of the shoaling and refraction of interfacial solitary waves in the ocean. Part I: Development of the model and investigations of the shoaling effect. J. Phys. Oceanogr., 31, 3163–3183, https://doi.org/10.1175/1520-0485(2001)031<3163:ANMOTS>2.0.CO;2.

- Spydell, M. S., and Coauthors, 2021: Internal bore evolution across the shelf near Pt. Sal, California, interpreted as a gravity current. *J. Phys. Oceanogr.*, 51, 3629–3650, https://doi.org/10.1175/JPO-D-21-00951.
- Stastna, M., and K. G. Lamb, 2002: Vortex shedding and sediment resuspension associated with the interaction of an internal solitary wave and the bottom boundary layer. *Geophys. Res. Lett.*, **29**, 1512, https://doi.org/10.1029/2001GL014070.
- Tyler, S. W., J. S. Selker, M. B. Hausner, C. E. Hatch, T. Torgersen, C. E. Thodal, and S. G. Schladow, 2009: Environmental temperature sensing using raman spectra dts fiberoptic methods. *Water Resour. Res.*, 45, W00D23, https://doi.org/10.1029/2008WR007052.
- Venayagamoorthy, S. K., and O. Fringer, 2005: Nonhydrostatic and nonlinear contributions to the energy flux budget in nonlinear internal waves. *Geophys. Res. Lett.*, 32, L15603, https:// doi.org/10.1029/2005GL023432.
- —, and O. B. Fringer, 2007: On the formation and propagation of nonlinear internal boluses across a shelf break. *J. Fluid Mech.*, 577, 137–159, https://doi.org/10.1017/S0022112007004624.
- Vlasenko, V., and K. Hutter, 2002: Numerical experiments on the breaking of solitary internal wavesover a slope-shelf topography. J. Phys. Oceanogr., 32, 1779–1793, https://doi.org/10.1175/ 1520-0485(2002)032<1779:NEOTBO>2.0.CO;2.
- Wallace, B., and D. Wilkinson, 1988: Run-up of internal waves on a gentle slope in a two-layered system. J. Fluid Mech., 191, 419–442, https://doi.org/10.1017/S0022112088001636.
- Walter, R. K., C. B. Woodson, R. S. Arthur, O. B. Fringer, and S. G. Monismith, 2012: Nearshore internal bores and turbulent mixing in southern Monterey Bay. *J. Geophys. Res.*, 117, C07017, https://doi.org/10.1029/2012JC008115.
- —, P. R. Leary, and S. G. Monismith, 2014: Connecting wind-driven upwelling and offshore stratification to nearshore internal bores and oxygen variability. *J. Geophys. Res. Oceans*, 119, 3517–3534, https://doi.org/10.1002/2014JC009998.
- Watanabe, Y., H. Saeki, and R. Hosking, 2005: Three-dimensional vortex structures under breaking waves. *J. Fluid Mech.*, **545**, 291–328, https://doi.org/10.1017/S0022112005006774.
- Winant, C. D., 1974: Internal surges in coastal waters. *J. Geophys. Res.*, **79**, 4523–4526, https://doi.org/10.1029/JC079i030p04523.
- Xu, C., and M. Stastna, 2020: Instability and cross-boundary-layer transport by shoaling internal waves over realistic slopes. *J. Fluid Mech.*, 895, R6, https://doi.org/10.1017/jfm.2020.389.
- —, C. Subich, and M. Stastna, 2016: Numerical simulations of shoaling internal solitary waves of elevation. *Phys. Fluids*, 28, 076601, https://doi.org/10.1063/1.4958899.